University of BRISTOL

Peer reviewed version

Link to published version (if available):
10.1038/s41586-018-0614-0

Link to publication record in Explore Bristol Research
PDF-document

University of Bristol - Explore Bristol Research
General rights

1 CO_2 storage and release in the deep Southern Ocean on

2 millennial to centennial timescales

3 Rae, J.W.B.[1,*], Burke, A.[1], Robinson, L.F.[2], Adkins, J.F.[3], Chen, T.[2,4], Cole,

4 C.[1], Greenop, R.[1], Li, T.[2,4], Littley, E.[1], Nita, D.C.[1,5], Stewart, J.A.[1,2], Taylor,

5 B[1].

6 1. School of Earth and Environmental Sciences, University of St Andrews, UK.

7 2. School of Earth Sciences, University of Bristol, UK

8 3. Division of Geological and Planetary Sciences, California Institute of

9 Technology, USA

10 4. School of Earth Sciences and Engineering, Nanjing University, China

11 5. Faculty of Environmental Science and Engineering, Babes-Bolyai

12 University, Cluj-Napoca, Romania

13

14 The cause of atmospheric CO_2 change during the recent ice ages remains a

15 first order question in climate science. Most mechanisms have invoked

16 carbon exchange with the deep ocean, due to its large size and relatively

17 rapid exchange time with the atmosphere [1]. The Southern Ocean is thought

18 to play a key role in this exchange, as much of the deep ocean is ventilated to

19 the atmosphere in this region [2]. However reconstructing changes in deep

20 Southern Ocean carbon storage is challenging, so **few direct tests of this**

21 **hypothesis exist. Here we present new deep-sea coral boron isotope**

22 **data that track the pH – and thus CO_2 chemistry – of the deep Southern**

23 **Ocean over the last 40,000 years. At sites closest to the Antarctic**

24 **continental margin, and most influenced by the deep Southern waters**

25 **that form the ocean's lower overturning cell, we find a close relationship**

26 **between ocean pH and atmospheric CO_2: during intervals of low CO_2**

27 **ocean pH is low, reflecting enhanced ocean carbon storage; during**

28 **intervals of rising CO_2 ocean pH rises, reflecting loss of carbon from the**

29 **ocean to the atmosphere. Correspondingly, at shallower sites we find**

30 **rapid (millennial to centennial-scale) pH decreases during abrupt CO_2**

31 **rise, reflecting the rapid transfer of carbon from the deep to the upper**

ocean and atmosphere. These data thus confirm the importance of the deep Southern Ocean in ice age CO_2 change, and demonstrate that deep ocean CO_2 release can occur as a dynamic feedback to rapid climate change on centennial timescales.

The Southern Ocean may act as a net source of CO_2 from the deep ocean to the atmosphere or a net sink [3], depending on the balance between regional CO_2-supply via circulation and CO_2-removal via biological productivity. Various records have shown that large changes in circulation [4,5] and biological productivity [6] occurred in the Southern Ocean on glacial timescales, with the potential to change the partitioning of carbon between the deep ocean and the atmosphere. However, reconstructions of deep ocean CO_2 storage are currently sparse and more complex. For instance records of CO_2 chemistry from the deep Atlantic [7] and deep Pacific [8] show decreases in carbonate ion saturation and pH during millennial-scale intervals of atmospheric CO_2 rise; in the absence of other processes, low carbonate ion and pH imply an increase in CO_2-storage in the deep ocean, so these signals are thought instead to be dominated by changes in circulation and deep water masses. On longer timescales, records from the deep Indo-Pacific [9] appear to reflect changes in CO_2-storage, but are damped by the buffering influence of carbonate compensation. Records of deep ocean CO_2 chemistry that clearly demonstrate CO_2 storage during atmospheric CO_2 fall, and CO_2 release during atmospheric CO_2 rise, have proved elusive.

Here we test the hypothesis that carbon storage in the deep Southern Ocean played a key role in ice age CO_2 change, with new boron isotope ($\delta^{11}B$) data from uranium-thorium dated deep-sea corals from the Drake Passage (Figure 1; Methods)[4]. The boron isotope pH proxy (see Methods) provides a sensitive measure of the ocean carbonate system, closely tracking CO_2 concentrations and reflecting the ratio of the two master variables, dissolved inorganic carbon (DIC) and alkalinity. Although full reconstruction of the carbonate system

2

64 requires knowledge of a second parameter, it is unlikely that alkalinity was

65 lower in the glacial ocean [10], or varied as dynamically as DIC, so our δ^{11}B-pH

66 record may be largely attributed to changes in carbon storage. Note that as

67 our δ^{11}B record extends beyond the pH calibration possible in modern *D.*

68 *dianthus* (Figure S5) we focus our discussion on relative changes in pH as

69 traced by coral δ^{11}B, and provide absolute pH estimates in Figure S1 for

70 reference. Our sample sites reflect distinct volumes of the deep ocean [11]: the

71 "lower cell" sites lie close to the Antarctic continental margin, bathed by

72 waters that plumb the mid to lower depths of the deep ocean; the "upper cell"

73 sites lie on lighter isopycnal surfaces, bathed by waters found at shallower

74 depths in the ocean basins (Figure 1).

75

76 During the LGM and early deglaciation we see a clear gradient between the

77 lower cell sites, which show low δ^{11}B and pH, and upper cell sites, with

78 relatively high δ^{11}B and pH (Figure 2). This supports the idea that during

79 glacial intervals the deep ocean – and its carbon – was more stratified into

80 two cells with limited interaction [11]. Our data show that the lower cell was rich

81 in carbon compared to the upper cell and compared to modern values

82 expected at this site (Figure 1, S1), providing strong support for the

83 hypothesis that the deep glacial ocean sequestered carbon from the upper

84 ocean and the atmosphere [2].

85

86 During the deglaciation this gradient in deep carbon breaks down, with lower

87 cell pH rising in step with atmospheric CO_2, and pH in the upper cell falling

88 towards lower cell values (Figure 3). This provides direct evidence for the

89 transfer of carbon from the deep ocean to the upper ocean and the

90 atmosphere. Carbon transfer to the upper ocean appears particularly

91 pronounced at ~14.7 and ~11.7 ka, coincident with the centennial-scale jumps

92 in atmospheric CO_2 [12] associated with abrupt warming in the Northern

93 Hemisphere. This provides the first evidence of a fast teleconnection

94 between abrupt changes in the North Atlantic and the carbon chemistry of the

95 deep Southern Ocean. Lower cell *D. dianthus* samples have not been found

96 in the Holocene (see Methods), but the available data at the end of the

97 deglaciation and in the modern water column suggest much weaker pH

98 gradients, consistent with less-pronounced property gradients in the modern

99 deep ocean compared to the glacial [11,13,14].

100

101 Our data show that the carbonate chemistry of the deep Southern Ocean was

102 closely linked to atmospheric CO_2 change over the last 40 ka. These data

103 thus provide a crucial missing piece of the glacial CO_2 puzzle: the most direct

104 evidence to date of deep Southern Ocean carbon storage and release, as

105 previously inferred from physical properties [5,13], carbon isotopes [15], and

106 oxygen content [16] (Figure 2 & S3). While other processes [3] and regions [8] may

107 contribute to the full magnitude of glacial-interglacial CO_2 change, our data

108 demonstrate a key role for the Southern Ocean on millennial to centennial

109 timescales.

110

111 Several processes may contribute to the changes in CO_2 storage observed in

112 our record, including changes in ventilation [4,16], biological pump efficiency [6],

113 and sea ice [17] (Figure S3). We note a close correspondence between lower

114 cell pH and ice core sea salt sodium, a proxy that may reflect changes in sea

115 ice production [18] [19] (Figure 2), suggesting that sea ice may play an important

116 role in CO_2 change. Sea ice has the potential to influence CO_2 storage both

117 through its influence as a "lid" on surface-ocean outgassing [17], and its impact

118 on deep circulation [11]. Expansion of sea ice at the LGM [11], alongside an

119 increase in surface ocean density in the Southern Ocean relative to the North

120 Atlantic [20], would help create an expanded lower cell with salty [13], CO_2-rich

121 water. This may shoal the upper/lower cell boundary above the zone of

122 enhanced mixing over rough bottom topography [11,14], trapping salt and CO_2 in

123 the abyss. Accumulation of CO_2 at depth would be further promoted by an

124 enhanced biological pump due to iron fertilization [6] and increased upper

125 ocean stratification, which would also reduce CO_2 escape through leads and

126 during ice-free conditions.

127

128 This framework may also explain release of CO_2 from the deep Southern

129 Ocean on millennial timescales [21]. CO_2 rise typically occurs during intervals

130 of cold stadial conditions in the Northern Hemisphere and warming in the

131 South (the bipolar seesaw) [22]. This southern warming is associated with a

132 decrease in Southern sea ice (Figures 2, 3) and a decrease in the Southern

133 Ocean to North Atlantic surface density gradient, shifting the boundary

134 between the overturning cells to greater depth in the basins [11] [20]. CO_2-rich

135 water previously isolated in the abyss may thus be mixed into the upper cell

136 over rough topography in the ocean basins, and/or transferred into the upper

137 cell upon upwelling North of the sea ice edge, perhaps aided by the westerly

138 winds [23,24] or increased mixed layer depths in the Southern Ocean. CO_2 loss

139 from the deep ocean may also aided by reduced biological pump efficiency [6].

140 Whatever the exact mechanism, this carbon transfer is recorded by a pH

141 increase in our lower cell corals and a pH decrease in our upper cell corals,

142 as CO_2 is transferred to the upper ocean and the atmosphere. Note that as a

143 southward shift in the fronts at these times might be expected to expose our

144 sites to higher-pH water (Figure 1), the transfer of low-pH DIC-rich water into

145 the upper cell may be even larger than observed. Indeed a southward frontal

146 shift and breakdown in stratification likely explain the younging seen in upper

147 cell radiocarbon [4,25] at this time (Figure S4). Upwelling of carbon and nutrient-

148 rich water during cold Northern Hemisphere stadials is also supported by low

149 pH in surface waters, as recorded by boron isotopes in planktic foraminifera

150 [26], and enhanced opal fluxes [23] (Figure 3 & S4). If salt from the high salinity

151 lower cell [13] is also transferred back into the upper cell, this may aid the re-

152 initiation of NADW formation [27]. Once interstadial conditions are

153 reestablished in the North Atlantic, the Southern Ocean starts to cool via the

154 bipolar seesaw and sea ice expands [28]. This shoals the cell boundary,

155 reduces ocean-atmosphere exchange, and allows CO_2 and salt to again

156 become trapped in the abyss (Figure 4).

157

158 The centennial-scale CO_2 jumps at 14.7 and 11.7 ka [12], which are associated

159 with pronounced minima in upper cell pH (Figure 3), appear to require a more

160 efficient mode of Southern Ocean CO_2 release associated with abrupt

161   Northern Hemisphere warming [25]. High-resolution records of Antarctic

162   deuterium excess indicate a northward shift in the Southern Westerly winds

163   synchronous with abrupt Northern Hemisphere warming [29]; in contrast the

164   bipolar seesaw cooling response in the south is lagged, with Antarctic $\delta^{18}O$

165   and sea salt sodium taking around 200 years to show the onset of cooling

166   conditions and increased sea ice production [28] (Figure 3). This may lead to a

167   transient condition in the Southern Ocean where CO_2 can be efficiently mixed

168   up from the lower cell [24], due to the fast shift in the winds, and then outgas

169   unimpeded by sea ice, which has not yet expanded [17]. The northward shift in

170   the fronts might also contribute to the pH minima by exposing our upper cell

171   sites to lower-pH water from the South (Figure 1), but such a shift would have

172   to be large given that upper cell pH appears to reach values similar to, or

173   even lower than, the lower cell at this time, suggesting increased input of CO_2-

174   rich water is required. Increased input of previously isolated carbon-rich

175   waters is also seen in radiocarbon data [4,25], which show an interruption of

176   their deglacial younging and a slight increase in age during these events

177   (Figure S4). Whatever the exact mechanisms involved, our data demonstrate

178   that the Southern Ocean may fill with CO_2-rich waters on centennial

179   timescales and may thus give out its carbon rapidly, countering suggestions

180   that centennial-scale CO_2 jumps are too quick for a deep ocean driver and

181   require exogenous carbon addition (such as from methane hydrates or the

182   terrestrial biosphere [30]). Our data show that rapid changes in the Southern

183   Ocean acted in concert with strong AMOC resumption [25] to drive rapid CO_2

184   rise.

185

186   Although our lower cell $\delta^{11}B$-pH data generally show a close coupling with

187   atmospheric CO_2, this relationship is somewhat muted during peak glacial

188   conditions, with pronounced minima in pH at ~26 and 20 ka, alongside

189   extensive sea ice [28], low upwelling [23], and an efficient biological pump [6]

190   (Figure S3), but minimal change in atmospheric CO_2. This supports the idea

191   of a lower limit on atmospheric CO_2 at ~190 ppm [31]: although Southern Ocean

192   carbon storage continues to increase, its influence on the atmosphere

193 appears to be offset by other processes, perhaps the onset of CO_2 limitation
194 on primary productivity on land [31].

195

196 Overall, our data provide a clear demonstration that storage and release of
197 CO_2 in the deep Southern Ocean plays a central role in glacial-interglacial
198 atmospheric CO_2 change. These changes in ocean CO_2 storage were likely
199 driven by a combination of changes in ocean circulation, biological pump
200 efficiency, and sea ice cover. We note a close correspondence between CO_2
201 storage and ice core sea ice sodium records, which may suggest that
202 Southern Ocean sea ice plays a key role, due to its joint influence on deep
203 overturning and surface outgassing. This provides a mechanistic explanation
204 for the tight link between Antarctic temperature and CO_2 change on glacial-
205 interglacial timescales, though several processes acting together are likely
206 required to explain the full magnitude of glacial CO_2 change. Our data also
207 highlight the ability of the Southern Ocean – and its CO_2 – to respond to
208 millennial and centennial-scale shifts in climate linked to the North Atlantic's
209 overturning circulation. Indeed, it is possible that the framework presented
210 here, which links the storage and release of deep ocean CO_2 and salt to
211 changes in Southern Ocean sea ice and the bipolar seesaw, may help
212 account for the occurrence of millennial-scale CO_2 and climate change during
213 mid-glacial conditions. At these times, moderate sea ice extent means that
214 the boundary between the ocean's lower and upper cells is located near the
215 top of rough seafloor topography. Small shifts in the cell boundary, linked to
216 changes in the Southern sea ice edge, may thus drive large shifts in the
217 degree of mixing between the lower and upper cells, and their salt and CO_2.
218 This framework may also give behavior similar to "density oscillator" models
219 for rapid climate change [27,32,33]: when AMOC is active and the Northern
220 Hemisphere warms, the South cools and sea ice expands, progressively
221 isolating cold salty water (and CO_2) in the lower cell. This may make the
222 AMOC vulnerable to collapse, at which point the South warms, sea ice
223 retreats, and the cell-boundary deepens. This helps mix salt (and CO_2) back
224 into the upper cell and makes the lower cell fresher and warmer, reducing the

225 deep ocean density contrast, and helping poise the system for AMOC

226 resumption.

227

References

1. Broecker, W. S. Glacial to interglacial changes in ocean chemistry. *Progress in Oceanography* **11,** 151–197 (1982).
2. Sarmiento, J. L. & Toggweiler, J. R. A new model for the role of the oceans in determining atmospheric pCO$_2$. *Nature* **308,** 621–624 (1984).
3. Sigman, D. M., Hain, M. P. & Haug, G. H. The polar ocean and glacial cycles in atmospheric CO$_2$ concentration. *Nature* **466,** 47–55 (2010).
4. Burke, A. & Robinson, L. F. The Southern Ocean's Role in Carbon Exchange During the Last Deglaciation. *Science* **335,** 557–561 (2012).
5. Roberts, J. *et al.* Evolution of South Atlantic density and chemical stratification across the last deglaciation. *PNAS* 201511252–14 (2016). doi:10.1073/pnas.1511252113
6. Martinez-Garcia, A. *et al.* Iron Fertilization of the Subantarctic Ocean During the Last Ice Age. *Science* **343,** 1347–1350 (2014).
7. Yu, J. *et al.* Deep South Atlantic carbonate chemistry and increased interocean deep water exchange during last deglaciation. *Quaternary Science Reviews* **90,** 80–89 (2014).
8. Rae, J. W. B. *et al.* Deep water formation in the North Pacific and deglacial CO2 rise. *Paleoceanography* **29,** 645–667 (2014).
9. Yu, J. *et al.* Responses of the deep ocean carbonate system to carbon reorganization during the Last Glacial--interglacial cycle. *Quaternary Science Reviews* **76,** 39–52 (2013).
10. Rickaby, R. E. M., Elderfield, H., Roberts, N., Hillenbrand, C. D. & Mackensen, A. Evidence for elevated alkalinity in the glacial Southern Ocean. *Paleoceanography* **25,** PA1209 (2010).
11. Ferrari, R. *et al.* Antarctic sea ice control on ocean circulation in present and glacial climates. *PNAS* **111,** 8753–8758 (2014).
12. Marcott, S. A. *et al.* Centennial-scale changes in the global carbon cycle during the last deglaciation. **514,** 616–619 (2014).
13. Adkins, J. F., McIntyre, K. & Schrag, D. P. The salinity, temperature, and δ^{18}O of the glacial deep ocean. *Science* **298,** 1769–1773 (2002).
14. Burke, A., Stewart, A. L., Adkins, J. F. & Ferrari, R. The glacial mid-depth radiocarbon bulge and its implications for the overturning circulation. *Paleoceanography* **30,** 1021–1039 (2015).
15. Charles, C. D. *et al.* Millennial scale evolution of the Southern Ocean chemical divide. *Quaternary Science Reviews* **29,** 399–409 (2010).
16. Jaccard, S. L., Galbraith, E. D., Martinez-Garcia, A. & Anderson, R. F. Covariation of deep Southern Ocean oxygenation and atmospheric CO$_2$ through the last ice age. *Nature* **530,** 207–210 (2016).
17. Stephens, B. B. & Keeling, R. F. The influence of Antarctic sea ice on glacial-interglacial CO$_2$ variations. *Nature* **404,** 171–174 (2000).
18. Wolff, E. W. *et al.* Southern Ocean sea-ice extent, productivity and iron flux over the past eight glacial cycles. *Nature* **440,** 491–496 (2006).
19. Abram, N. J., Wolff, E. W. & Curran, M. A. J. A review of sea ice proxy information from polar ice cores. *Quaternary Science Reviews* **79,** 168–183 (2013).
20. Galbraith, E. & de Lavergne, C. Response of a comprehensive climate

276   model to a broad range of external forcings: relevance for deep ocean
277   ventilation and the development of late Cenozoic ice ages. *Climate*
278   *Dynamics* 1–27 (2018). doi:10.1007/s00382-018-4157-8

21. Ahn, J. & Brook, E. J. Atmospheric CO_2 and Climate on Millennial Time Scales During the Last Glacial Period. *Science* **322,** 83–85 (2008).

22. Stocker, T. F. The seesaw effect. *Science* (1998).

23. Anderson, R. F. *et al.* Wind-Driven Upwelling in the Southern Ocean and the Deglacial Rise in Atmospheric CO_2. *Science* **323,** 1443–1448 (2009).

24. Abernathey, R. & Ferreira, D. Southern Ocean isopycnal mixing and ventilation changes driven by winds. *Geophysical Research Letters* **42,** 10,357–10,365 (2015).

25. Chen, T. *et al.* Synchronous centennial abrupt events in the ocean and atmosphere during the last deglaciation. *Science* **349,** 1537–1541 (2015).

26. Martínez-Botí, M. A. *et al.* Boron isotope evidence for oceanic carbon dioxide leakage during the last deglaciation. *Nature* **518,** 219–222 (2015).

27. Broecker, W. S., Bond, G., Klas, M., Bonani, G. & Wolfli, W. A salt oscillator in the glacial Atlantic? 1. The concept. *Paleoceanography* **5,** 469–477 (1990).

28. Members, W. D. P. *et al.* Precise interpolar phasing of abrupt climate change during the last ice age. *Nature Publishing Group* **520,** 661–16 (2015).

29. Markle, B. R. *et al.* Global atmospheric teleconnections during Dansgaard-Oeschger events. *Nature Geoscience* **10,** 36–40 (2017).

30. Köhler, P., Knorr, G. & Bard, E. Permafrost thawing as a possible source of abrupt carbon release at the onset of the Bølling/Allerød. *Nature Communications* **5,** 1–10 (2014).

31. Galbraith, E. D. & Eggleston, S. A lower limit to atmospheric CO_2 concentrations over the past 800,000 years. *Nature Geosci* **10,** 295–298 (2017).

32. Bereiter, B., Shackleton, S., Baggenstos, D., Kawamura, K. & Severinghaus, J. Mean global ocean temperatures during the last glacial transition. *Nature Publishing Group* **553,** 39–44 (2018).

33. Keeling, R. F. & Stephens, B. B. Antarctic sea ice and the control of Pleistocene climate instability. *Paleoceanography* (2001).

314

315
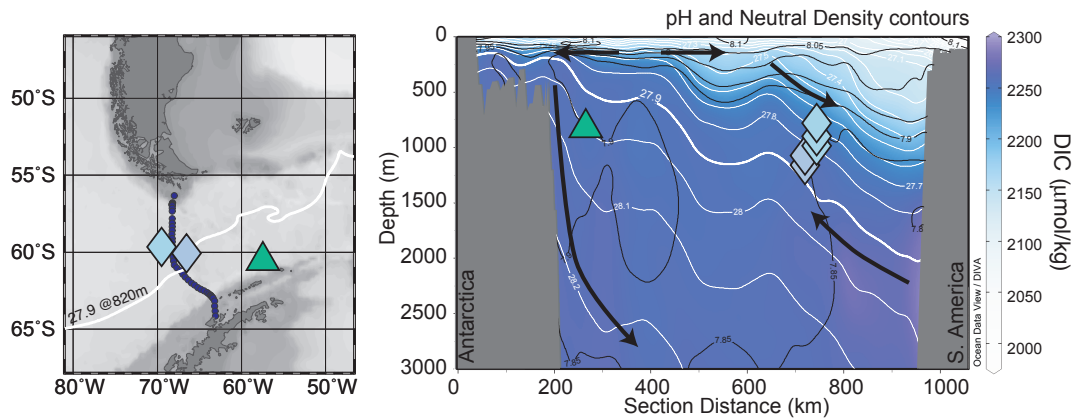
Figure 1: Locations of deep-sea coral samples. The cross section (right
panel) is constructed from hydrographic stations across the Drake Passage
(dark blue dots on map, left panel). Steeply dipping isopycnals in this region
(white contours) mean our sites fall into two groups spanning distinct volumes
of the deep ocean [11]. The green triangle marks the lower cell sites, which lie
close to the Antarctic continental margin in the Shackleton Fracture Zone; the
blue diamonds the upper cell sites, which lie at lower densities on the Sars
(lighter blue) and Interim (darker blue) seamounts. Lower cell waters are rich
in DIC (shading, right panel) with low pH (black contours); upper cell waters
have higher pH and are more closely connected to the atmosphere. Coral
locations on the section are given in coordinates of depth and neutral density,
based on CTD data collected alongside the coral dredges. Note that there is
no significant offset in our $\delta^{11}B$ data between upper cell corals from different
depths (Figure S2), and that differences in pH between these sites are small
compared to the range seen in our records. The 27.9 neutral density contour
in the map view (left) is shown at 820 m, the average depth of our corals.
Section data are from GLODAPv2 [34,35], plotted using isopycnal gridding in
Ocean Data View.

334

335
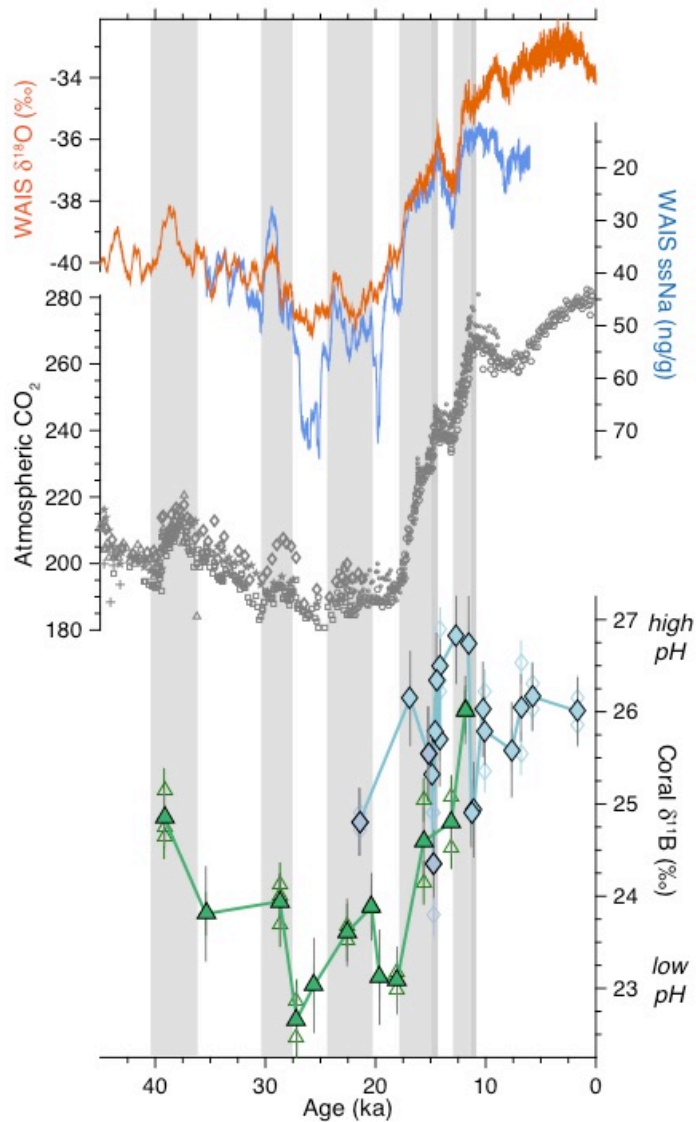
Figure 2: Deep Southern Ocean CO$_2$ chemistry, atmospheric CO$_2$, and Antarctic climate records over the last 40,000 years. Green triangles and blue diamonds show lower and upper cell deep-sea coral δ^{11}B data respectively. Individual subsamples are shown in small open symbols and mean values in larger filled symbols. Error bars on individual subsamples are equivalent to 2 SD analytical reproducibility and error bars on mean coral values represent 2 SE uncertainty on the mean of replicate subsamples (see Methods). Synchronised ice core CO$_2$ data [36] are shown in grey symbols: circles from Dome C, dots from WAIS, stars from Taylor Dome, triangles from TALDICE, pluses from EDML, diamonds from Byrd, and squares from Siple Dome. WAIS δ^{18}O (orange line), which reflects Antarctic temperature, and sea salt sodium (blue line), a proxy for sea ice, have been smoothed with a running mean [28]. Grey bands highlight intervals of CO$_2$ rise.

349

350
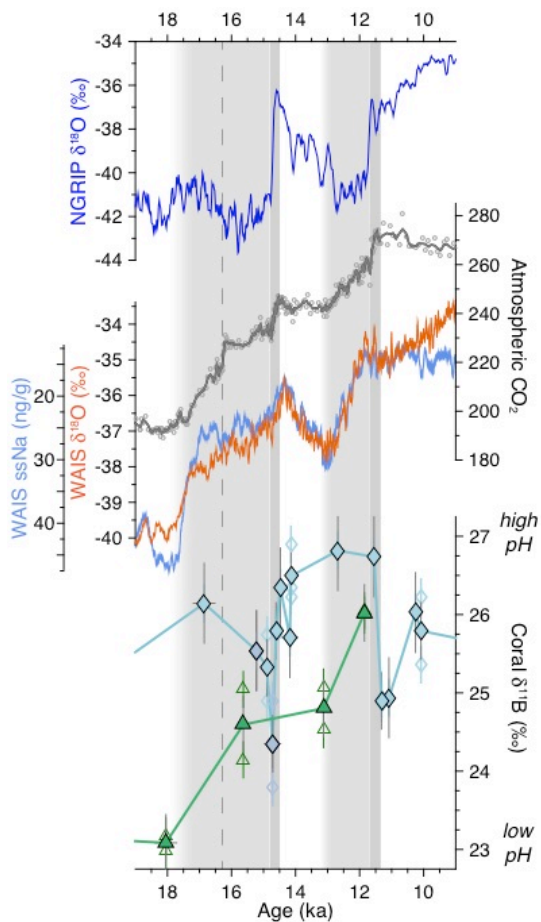
Figure 3: Deglacial records of deep Southern Ocean CO₂ chemistry, atmospheric CO₂, and climate over Antarctica and Greenland. Green triangles and blue diamonds show lower and upper cell deep-sea coral $\delta^{11}B$ data respectively. Individual subsamples are shown in small open symbols and mean values in larger filled symbols. Error bars on individual subsamples are equivalent to 2 SD analytical reproducibility and error bars on mean coral values represent 2 SE uncertainty on the mean of replicate subsamples (see Methods). Greenland ice core $\delta^{18}O$ (dark blue line), WAIS $\delta^{18}O$ (orange line), and sea salt sodium (blue line), have been smoothed with a running mean [28]. CO₂ data (grey symbols) are from WAIS [12] with a 5-point running mean (grey line). Light grey vertical bands highlight intervals of millennial-scale CO₂ rise; dark grey vertical bands highlight intervals of centennial-scale CO₂ rise associated with North Hemisphere warming, and the vertical dashed line indicates the rapid CO₂ rise event that occurs at 16.3 ka, within Heinrich Stadial 1.
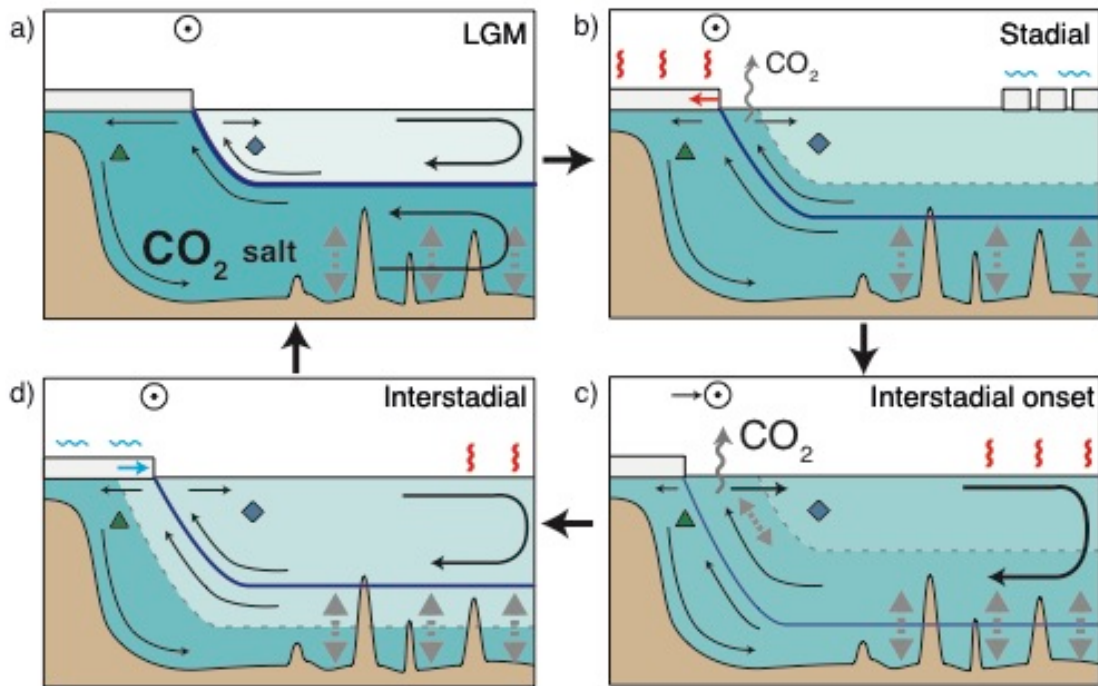
366

Figure 4

a) At the LGM extensive Southern Ocean sea ice creates an expanded lower cell with salty, CO_2-rich water. The cell boundary is shoaled above the zone of enhanced mixing over rough bottom topography, isolating salt and CO_2 in the abyss.

b) During a Northern Hemisphere stadial event, North Atlantic overturning is reduced, the Southern Ocean warms, and sea ice retreats. This shifts the cell boundary such that water previously isolated in the lower cell now upwells North of the sea ice edge. This water – and its CO_2 and salt – are transferred to the upper ocean and CO_2 outgases to the atmosphere. Transfer of salt from the lower to the upper cell may help re-initiate NADW formation.

c) At the onset of a Northern Hemisphere interstadial event (e.g. Bølling-Allerød, end Younger Dryas), resumption of NADW warms the Northern Hemisphere and leads to a rapid Northward shift in the Westerly winds; the Southern Ocean temperature and sea ice response is slower. This creates a transient condition where sea ice is unable to shield the ocean from enhanced isopycnal mixing nor the atmosphere from enhanced outgassing, leading to centennial-scale CO_2 rise.

d) As the interstadial continues, the Southern Ocean cools and sea ice expands. This shoals the cell boundary and allows salt and carbon to again become trapped in the abyss.

Climate states with moderate sea ice extent, where the cell boundary hovers around the top of rough seafloor topography, may give favourable conditions for rapid climate and CO_2 change, as the ocean flips between modes of connection vs isolation of the upper and lower cells.

14

Acknowledgements

Author Contributions

J.W.B.R., A.B., and L.F.R. designed the study. A.B., L.F.R., T.C., and T.L. collected and uranium-thorium dated the coral samples. J.W.B.R., B.T., E.L., C.C., J.S., and D.C.N. made boron isotope analyses. All authors contributed to the interpretation and the preparation of the manuscript.

The authors declare no competing interests.

Correspondence and requests for materials should be addressed to J.W.B.R (jwbr@st-andrews.ac.uk)

Methods

Sample collection and chronology

Deep-sea coral samples were collected by dredge during two cruises in the Drake Passage (NBP0805 and NBP1103). A total of 392 *D. dianthus* samples were initially "reconnaissance" dated, either by ^{14}C [37,38] or laser ablation U-Th [25,39], to obtain preliminary ages. Suitable samples with ages within the last ~50 ka were then precisely dated by isotope dilution U-Th by MC-ICPMS [4,25]. All ages have been published previously, and have typical uncertainties of around ±1 % (2 SD), though this varies between samples depending on their initial ^{230}Th (calculated from measured ^{232}Th and assuming an initial atomic ^{232}Th/^{230}Th ratio of 12,500 ± 12,500). Age errors are plotted in all time series figures but are typically smaller than the symbols. This precisely-dated and unbioturbated deep sea archive provides a unique record of ocean pH change at resolution comparable to the ice cores.

Sample preparation

Coral pieces were sampled from the growing tip of coral septa. Samples were physically cleaned using a Dremmel tool to remove all visible iron-manganese oxides and any chalky white carbonate, indicative of alteration.

We tested the potential influence of microstructural variability on coral δ^{11}B with multiple solid sub-samples from the same coral (Figure S6). Coral centres of calcification have previously been observed to have anomalously light boron isotope values, along with high Mg/Ca and low U/Ca [40-44], and we observe this same coupled variability in our coral subsamples (Figure S6). However this microstructural signal is typically small compared to the size of the boron isotope signals seen in our record. We had expected the smaller subsamples to exhibit more scatter, due to the potential influence of coral centers of calcification (COCs), but this is not shown in these data. There is in fact slightly more variability between larger chunks, perhaps due to the increased chance of sampling some COC material. For our records we used

449 coral pieces of ~1 mg. We also mitigated microstructural influences by taking

450 multiple solid subsamples from each coral when possible (shown as open

451 symbols). Two subsamples (at 1.6 ka and 20.4 ka) were rejected from our

452 total set of 55 as having anomalous $\delta^{11}B$ values (~1 ‰ lighter than the mean

453 of 3-4 other subsamples from that coral), which may be due to the impact of

454 COC material.

455

456 **Boron isotope analysis**

457 Solid coral samples were crushed to a grain size <1 mm using an agate pestle

458 and mortar. Samples were then subjected to oxidative cleaning to remove

459 organic matter following established protocols [45-48], using warm 1 % hydrogen

460 peroxide, buffered in 0.1 M NH_4OH, followed by leaching in 0.0001 M HNO_3,

461 and dissolution in 0.075 M distilled HNO_3. Boron was purified from the

462 sample matrix using column chromatography with the boron-specific ion

463 exchange resin Amberlite 743 [49-51].

464 Boron isotope composition was analysed by MC-ICPMS by sample-standard

465 bracketing [47,48,51]. Early analyses used NH_3 to improve boron washout in the

466 spray chamber [52], which reduces background signals to ~3 % of the

467 preceding sample within ~3 minutes [51]. More recent analyses used dilute HF

468 [53], which reduces background signals to ~0.5 % within ~3 minutes. In

469 contrast to some previous work, where samples are analysed in pure 0.3 M

470 HF [53], we add a small volume of concentrated HF to our sample following

471 column elution in 0.5 M HNO_3, giving a solution of 0.5 M HNO_3 + 0.3 M HF.

472 Similarly, bracketing standards (NIST 951) and instrument blank acid were

473 analysed in 0.5 M HNO_3 + 0.3 M HF to ensure consistent mass bias and blank

474 corrections, though beyond improved washout we do not find any significant

475 influence of HF concentration: boric acid standards run as dummy-samples

476 run with HF concentrations from 0 to 0.5 M HF bracketed against 951 in 0.5 M

477 HNO_3 + 0.3 M HF all yield identical boron isotope ratios. Carbonate

478 standards (JCP, NIST RM8301C) passed through columns and run with NH_3

479 or HF also yield identical values.

480   All preparation and analytical work was carried out in boron-free clean
481   laboratory conditions. Over the course of this work samples were analysed at
482   the University of Bristol and Caltech on a Neptune MC-ICPMS, and the
483   University of St Andrews on a Neptune Plus MC-ICPMS, though in all cases
484   following nearly identical protocols. Each of these laboratories has taken part
485   in published and ongoing inter-laboratory comparison studies [48] and there is
486   no analytical offset between samples run in these laboratories.

487   Long-term analytical reproducibility on $\delta^{11}B$ measurements in these
488   laboratories (assessed with carbonate standards given the same treatment as
489   samples) is around 0.23 ‰ (2 SD) on samples of the size used here (~20 ng
490   boron) – this is the error bar given on individual subsamples (open symbols in
491   figures). We use a more conservative uncertainty for our mean coral $\delta^{11}B$
492   values (filled symbols in figures), to account for the $\delta^{11}B$ variability between
493   subsamples from the same coral. This is based on the pooled standard
494   deviation of the replicate samples in our records and in Figure S6 (2 SD =
495   0.51 ‰). Uncertainty is reduced on mean values with multiple replicates (n),
496   which is accounted for using the standard error (SD/$\sqrt{n}$).

497

498   **$\delta^{11}B$ and pH in deep-sea corals**

499   The boron isotope pH proxy provides a sensitive measure of the ocean
500   carbonate system, though in common with many proxies, is also influenced by
501   modification during biomineralisation [54-57]. In particular, coral $\delta^{11}B$ is
502   influenced by internal pH-elevation during biomineralisation [58,59], which may
503   buffer its sensitivity to external seawater pH changes in some settings. To
504   examine this we have compiled modern *D. dianthus* $\delta^{11}B$ calibration data
505   [44,56,60] from water depths >100 m, and have added two recent Southern
506   Ocean samples. This indicates that the relationship between seawater pH
507   and coral $\delta^{11}B$ is curved, with $\delta^{11}B$ becoming more sensitive to external
508   seawater at lower pH (Figure S5). This suggests that corals find it harder to
509   elevate internal pH as external conditions become more acidic, which is
510   reasonable, given the increase in energy demand required for additional
511   proton expulsion [61]. It also means that corals are likely to be more sensitive to

512   external pH conditions at lower pH sites, such as the Southern Ocean
513   locations in this study. Hence, the pH changes that occured during the last
514   40,000 yr are evident as large, easily resolvable changes in δ^{11}B in our coral
515   record.

516   Reconstructed pH based on this calibration is shown in Figure S1. Given the
517   paucity of modern deep-sea coral samples from low-pH waters, our record
518   extends beyond the available calibration range. As a result conversion to
519   absolute pH values carries relatively large uncertainty, which is hard to
520   assess. We thus prefer to focus on relative changes in the δ^{11}B records
521   themselves, which provide a proxy of carbonate chemistry in their own right [62],
522   analogous to the typical use of δ^{18}O records in paleoceanography.
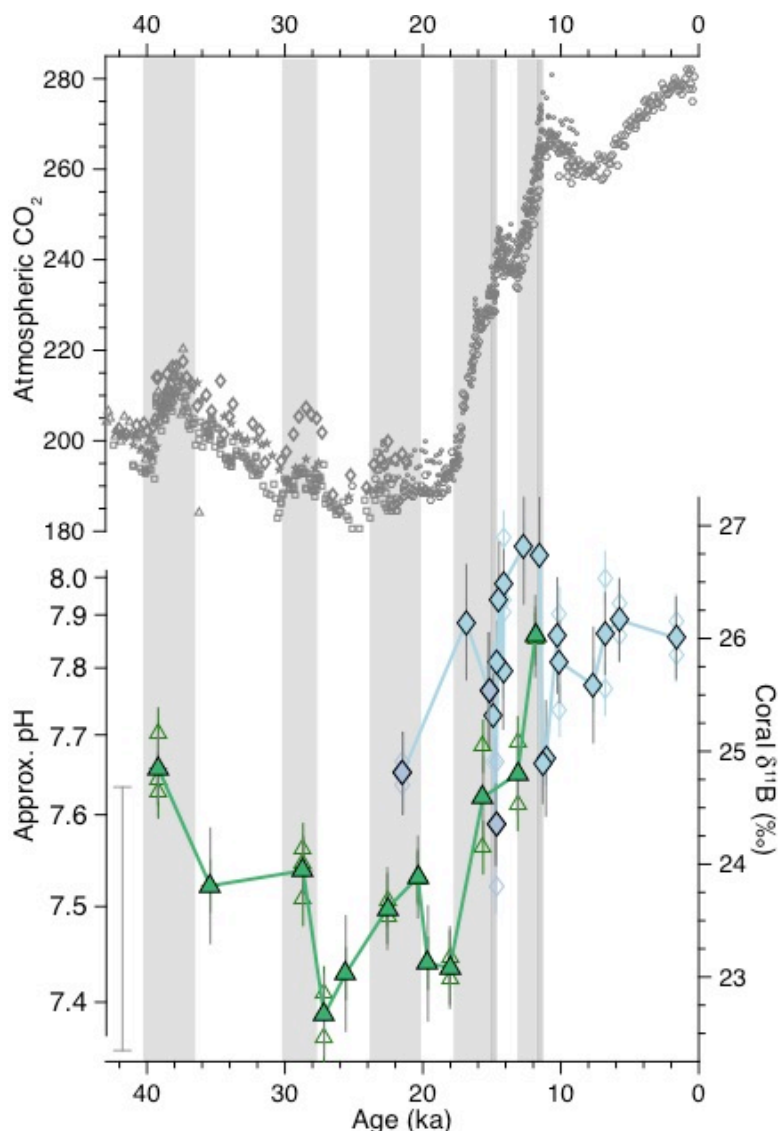
523

524   **Data availability**

525   The data produced in this study is available as a supplementary table and will
526   also be made available at the NOAA and Pangaea data repositories.

527

Supplementary Figures

Figure S1: Deep Southern Ocean CO₂ chemistry and atmospheric CO₂ over the last 40,000 years. Green triangles and blue diamonds show lower and upper cell deep-sea coral δ^{11}B data respectively. Individual subsamples are shown in small open symbols and mean values in larger filled symbols. Error bars on individual subsamples are equivalent to 2 SD analytical reproducibility and error bars on mean coral values represent 2 SE uncertainty on the mean of replicate subsamples (see Methods). Approximate pH values are given based on coral δ^{11}B using the calibration in Figure S5, but uncertainty on this calibration is large (inset error bar), given the paucity of modern deep-sea coral data from low pH waters. Instead we focus on the δ^{11}B values themselves, which provide a proxy of carbonate chemistry in their own right [62]. Synchronised ice core CO₂ data [36] are shown in grey symbols: circles from Dome C, dots from WAIS, stars from Taylor Dome, triangles from TALDICE, pluses from EDML, diamonds from Byrd, and squares from Siple Dome. Grey bands highlight intervals of CO₂ rise.
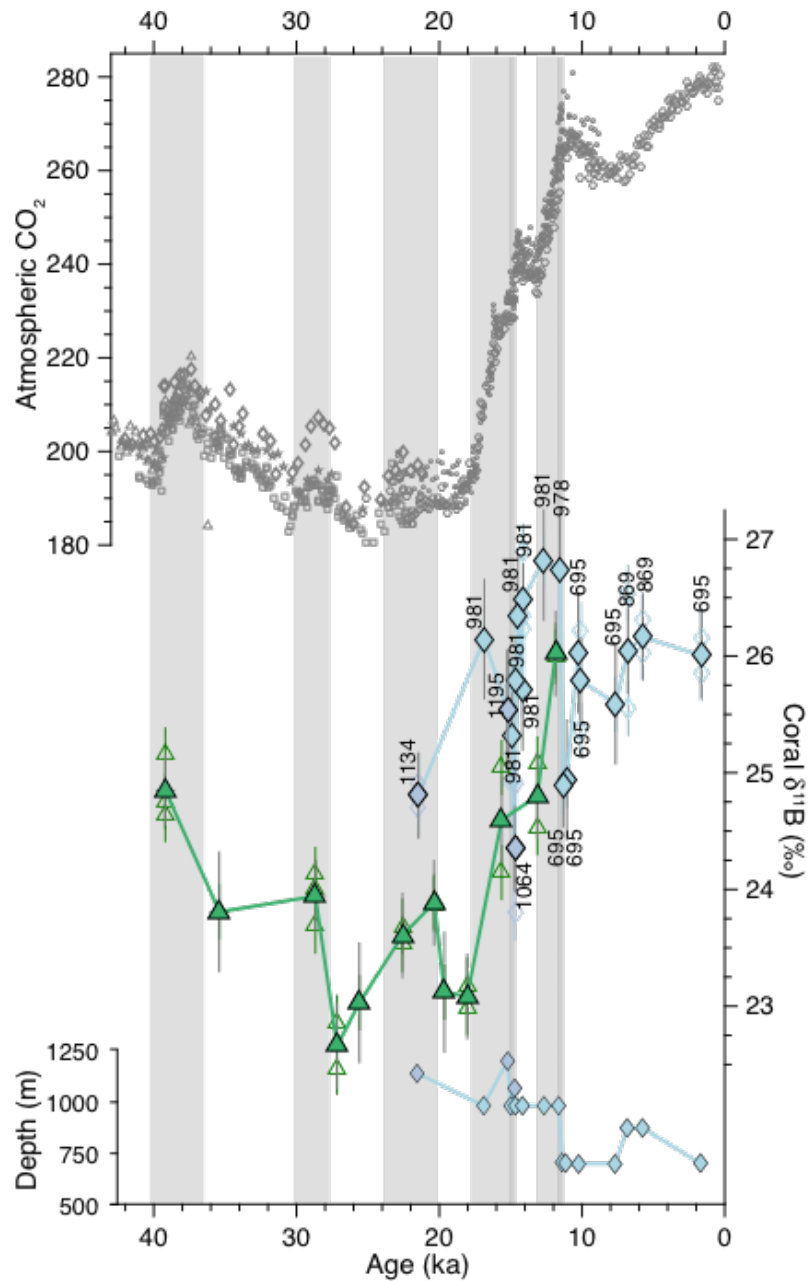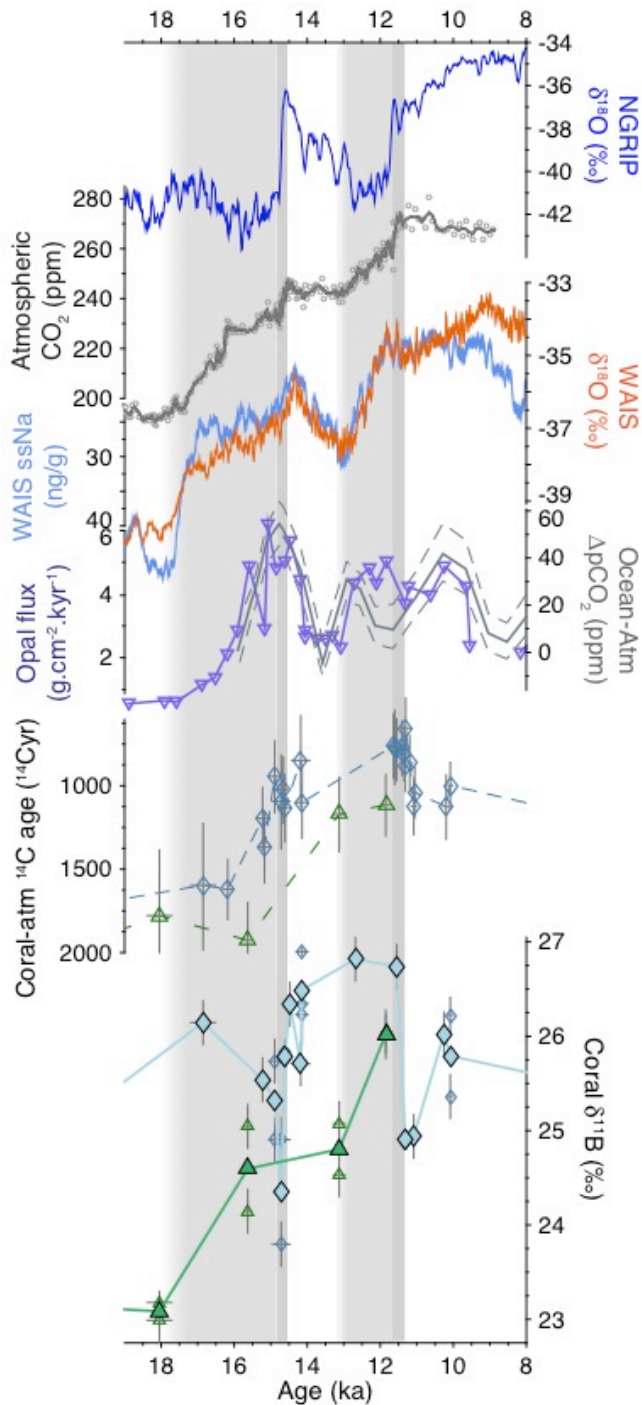
Figure S2: Deep Southern Ocean CO₂ chemistry and atmospheric CO₂ over the last 40,000 years, highlighting the depths of upper cell corals. Symbols and data are as plotted in Figure S1, but with the addition of the lower panel and annotations showing the depth in meters of each upper cell coral sample. No systematic offset is seen between samples from different depths. The only signal that occurs simultaneous with a change in depth is the decrease at ~11.5 ka, but the jump back up to higher $\delta^{11}B$ values following this event occurs without a change in depth, giving confidence that the excursion is not a depth-related signal. Furthermore the large excursion at ~14.7 ka occurs without a significant change in depth. Note that all of the lower cell corals come from within 17 m water depth of each other.

558
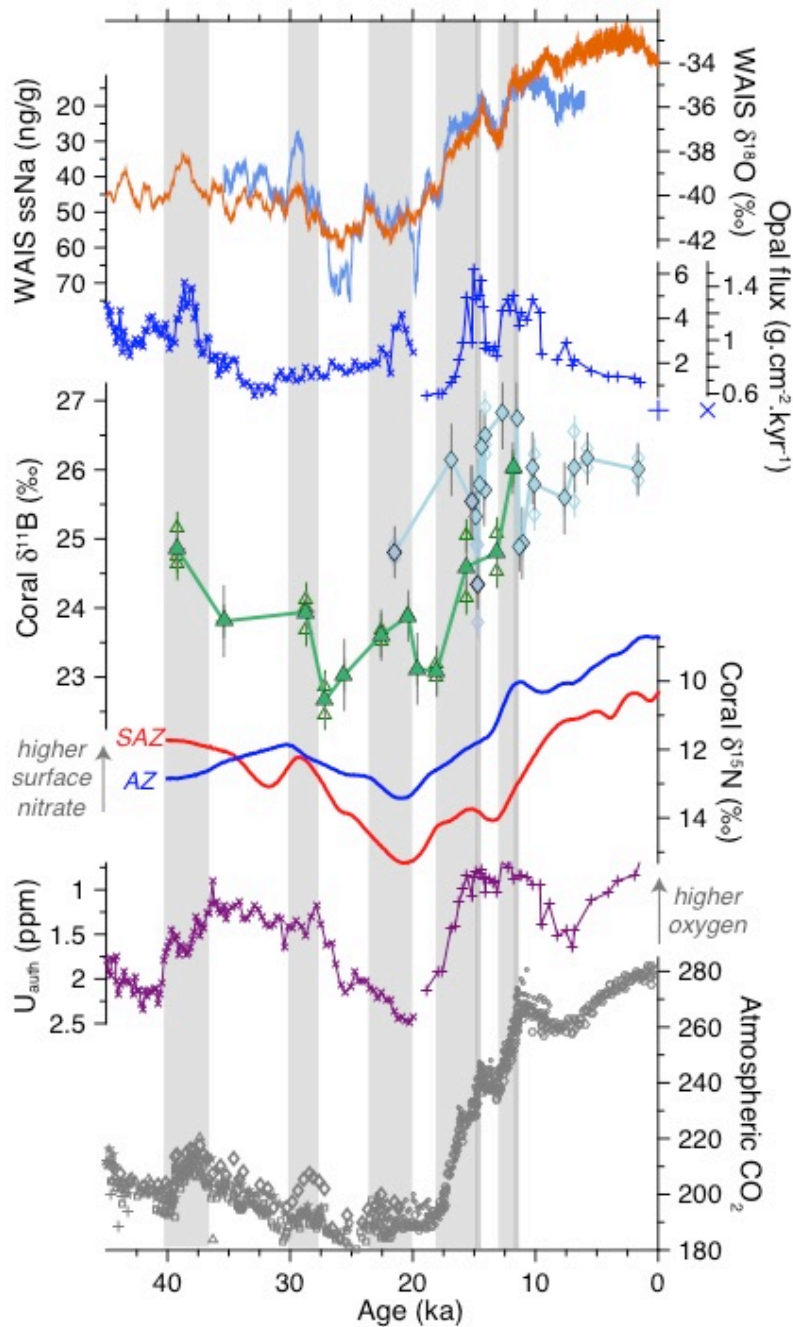
559
560 **Figure S3: Records of Southern Ocean biogeochemistry and CO$_2$ over**
561 **the last 40,000 yr.** Data are plotted as in Figure 2, but with opal flux [23], a
562 proxy for upwelling, deep sea coral δ^{15}N [63], a proxy for surface ocean nitrate
563 consumption, and authigenic uranium concentrations [16], a proxy for bottom
564 water redox. The opal flux and authigenic uranium records combine two
565 sediment cores: TN057-13-4PC in the younger part of the record (pluses) and
566 TN057-14PC in the older part of the record (crosses). The opal flux records
567 from each core are shown on separate scales. The coral δ^{15}N data are grouped
568 into samples from the Antarctic Zone (AZ, blue) and Subantarctic Zone (SAZ, red).
569 Smoothed fits to the data are shown, as provided in the original study [63]. Intervals
570 of low CO$_2$ during the last ice age are associated with low upwelling, an
571 efficient biological pump, low oxygen water rich in respired carbon, and low-
572 pH carbon-rich water in the deep Southern Ocean.

Figure S4: Deglacial records of Southern Ocean CO₂ chemistry and opal fluxes, and climate over Antarctica and Greenland. Data are plotted as in Figures 2 and 3, but with opal flux [23], a proxy for upwelling, surface ocean-atmosphere CO_2 difference, based on $\delta^{11}B$ in planktic foraminifera [26], and radiocarbon data [4,25] from corals within these sample groupings, shown as age offsets compared to the contemporaneous atmosphere. Intervals of rising CO_2 in the atmosphere are associated with input of waters rich in CO_2 and nutrients to the upper reaches of the Southern Ocean. Radiocarbon ages reflect the competing influences of upwelling of ^{14}C-depleted waters and improved ventilation over the deglaciation.

585
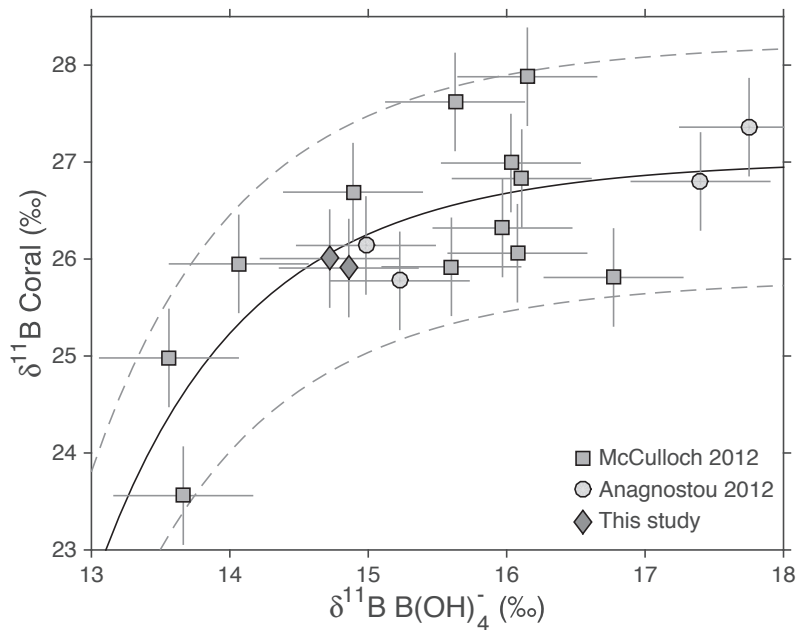
586
587 **Figure S5: Boron isotope calibration for modern *D. dianthus*.** Data are
588 from open ocean sites in [44,56,60], with two additional recent (<1650 yr) samples
589 from the Southern Ocean from this study. Water column δ^{11}B of borate
590 (B(OH)$_4^-$) values are as previously published or are calculated from carbonate
591 chemistry data from nearby GLODAPv2 sites for the new samples, following
592 [47,62]. Note that the sensitivity of δ^{11}B in carbonates to pH is based on the pH
593 sensitivity of δ^{11}B of borate. pH itself is not easily shown on a plot like this, as
594 the relationship between δ^{11}B of borate and pH is also somewhat influenced
595 by water temperature, salinity, and depth. A power law function was fitted to
596 the data using Matlab's curve fitting toolbox (solid line: δ^{11}B$_{Coral}$ = -1.82^{14} x
597 δ^{11}B$_{B(OH)4-}$$^{-12.22}$ + 27.03; R^2 = 0.57). Dashed lines show the 95 % confidence
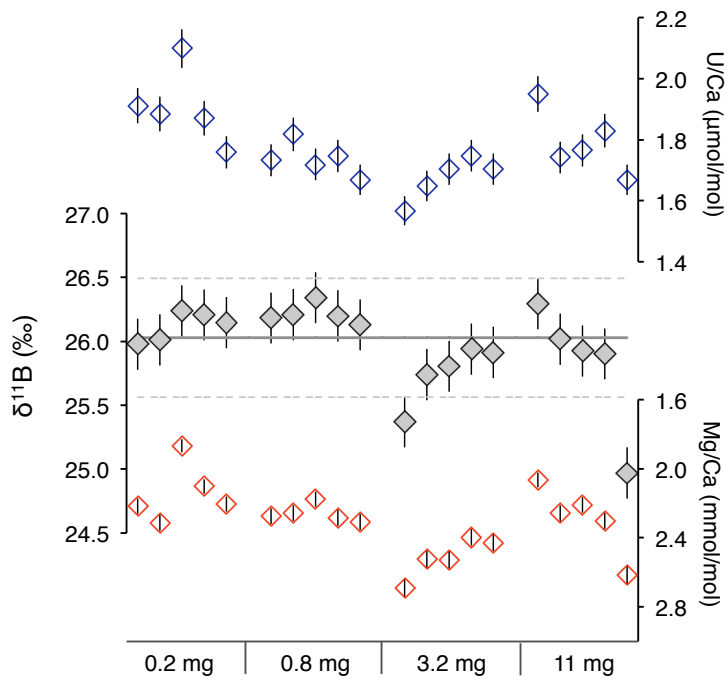598 intervals and give a measure of calibration uncertainty as shown in the error
599 bar in Figure S1, though data from a given site may be able to record relative
600 changes in pH more sensitively, as seen in many paleo-proxies.
601

602

603
604
Figure S6: Replicate subsamples from a *D. dianthus* septum. To test for
the potential influence of microstructural variability in composition, a coral
septum was divided into 4 areas, which were then split into chunks of
approximately 0.2, 0.8, 3.2 and 11 mg respectively. These were then
individually crushed, cleaned, and analysed. This sample treatment was
designed to preserve heterogeneity between subsamples, though note that
the clustering of subsamples of a given size from a certain area of the coral
may lead to that group recording a slightly different signal (as seen in the 3.2
mg group). The lines in the middle panel show the mean and 2 SD, excluding
one outlier in the 11 mg group. $\delta^{11}B$ is correlated with Mg/Ca and U/Ca,
showing the influence of internal variability in coral composition.

616

Additional References

34. Key, R. M. *et al.* Global Ocean Data Analysis Project, Version 2 (GLODAPv2). *EPIC3ORNL/CDIAC-162, NDP-093, Carbon Dioxide Information Analysis Center, Oak Ridge Nat Lab* (2015). doi:10.3334/CDIAC/OTG

35. Olsen, A. *et al.* The Global Ocean Data Analysis Project version 2 (GLODAPv2) – an internally consistent data product for the world ocean. *Earth System Science Data* **8,** 297–323 (2016).

36. Bereiter, B. *et al.* Revision of the EPICA Dome C CO_2 record from 800 to 600 kyr before present. *GRL* **42,** 542–549 (2015).

37. Burke, A. *et al.* Reconnaissance dating: A new radiocarbon method applied to assessing the temporal distribution of Southern Ocean deep-sea corals. *Deep Sea Research Part I: Oceanographic Research Papers* **57,** 1510–1520 (2010).

38. Margolin, A. R. *et al.* Temporal and spatial distributions of cold-water corals in the Drake Passage: Insights from the last 35,000 years. *Deep Sea Research Part II: Topical Studies in Oceanography* **99,** 237–248 (2014).

39. Spooner, P. T., Chen, T., Robinson, L. F. & Coath, C. Rapid uranium-series age screening of carbonates by laser ablation mass spectrometry. *Quaternary Geochronology* **31,** 28–39 (2016).

40. Sinclair, D. J., Kinsley, L. P. & McCulloch, M. T. High resolution analysis of trace elements in corals by laser ablation ICP-MS. *Geochim. Cosmochim. Acta* **62,** 1889–1901 (1998).

41. Robinson, L. F. *et al.* Primary U distribution in scleractinian corals and its implications for U series dating. *Geochem. Geophys. Geosyst. (G3)* **7,** Q05022 (2006).

42. Gagnon, A. C., Adkins, J. F., Fernandez, D. P. & Robinson, L. F. Sr/Ca and Mg/Ca vital effects correlated with skeletal architecture in a scleractinian deep-sea coral and the role of Rayleigh fractionation. *EPSL* **261,** 280–295 (2007).

43. Rollion-Bard, C., Chaussidon, M. & France-Lanord, C. Biological control of internal pH in scleractinian corals: Implications on paleo-pH and paleo-temperature reconstructions. *Comptes rendus - Geoscience* **343,** 397–405 (2011).

44. Stewart, J. A., Anagnostou, E. & Foster, G. L. An improved boron isotope pH proxy calibration for the deep-sea coral *Desmophyllum dianthus* through sub-sampling of fibrous aragonite. *Chemical geology* **447,** 148–160 (2016).

45. Boyle, E. A. Cadmium, zinc, copper, and barium in foraminifera tests. *EPSL* **53,** 11–35 (1981).

46. Barker, S., Greaves, M. & Elderfield, H. A study of cleaning procedures used for foraminiferal Mg/Ca paleothermometry. *Geochem. Geophys. Geosyst.* **4,** 8407 (2003).

47. Rae, J. W. B., Foster, G. L., Schmidt, D. N. & Elliott, T. Boron isotopes and B/Ca in benthic foraminifera: Proxies for the deep ocean carbonate system. *EPSL* **302,** 403–413 (2011).

666   48.   Foster, G. L. *et al.* Interlaboratory comparison of boron isotope analyses
667   of boric acid, seawater and marine $CaCO_3$ by MC-ICPMS and NTIMS.
668   *Chem. Geol.* **358,** 1–14 (2013).

669   49.   Kiss, E. Ion-exchange separation and spectrophotometric determination
670   of boron in geological materials. *Analytica Chimica Acta* **211,** 243–256
671   (1988).

672   50.   Lemarchand, D., Gaillardet, J., Göpel, C. & Manhès, G. An optimized
673   procedure for boron separation and mass spectrometry analysis for
674   river samples. *Chemical geology* **182,** 323–334 (2002).

675   51.   Foster, G. L. Seawater pH, pCO_2 and $[CO_3^=]$ variations in the Caribbean
676   Sea over the last 130 kyr: A boron isotope and B/Ca study of planktic
677   foraminifera. *EPSL* **271,** 254–266 (2008).

678   52.   Al-Ammar, A. S., Gupta, R. K. & Barnes, R. M. Elimination of boron
679   memory effect in inductively coupled plasma-mass spectrometry by
680   ammonia gas injection into the spray chamber during analysis.
681   *Spectrochimica Acta Part B: Atomic Spectroscopy* **55,** 629–635 (2000).

682   53.   Misra, S., Owen, R., Kerr, J. & Greaves, M. Determination of $\delta^{11}B$ by
683   HR-ICP-MS from mass limited samples: Application to natural
684   carbonates and water samples. *Geochemica et Cosmochimica Acta*
685   **140,** 531–552 (2014).

686   54.   Rae, J. W. B. in *Boron Isotopes* 107–143 (Springer, 2018).

687   55.   McCulloch, M. T. *et al.* in *Boron Isotopes* 145–162 (Springer, 2018).

688   56.   Anagnostou, E., Huang, K. F., You, C. F., Sikes, E. L. & Sherrell, R. M.
689   Evaluation of boron isotope ratio as a pH proxy in the deep sea coral
690   *Desmophyllum dianthus*: Evidence of physiological pH adjustment.
691   *EPSL* **349-350,** 251–260 (2012).

692   57.   Trotter, J. *et al.* Quantifying the pH `vital effect' in the temperate
693   zooxanthellate coral Cladocora caespitosa: Validation of the boron
694   seawater pH proxy. *EPSL* **303,** 163–173 (2011).

695   58.   Venn, A. A. *et al.* Impact of seawater acidification on pH at the tissue-
696   skeleton interface and calcification in reef corals. *PNAS* **110,** 1634–
697   1639 (2013).

698   59.   Allison, N., Cohen, I., Finch, A. A., Erez, J. & Tudhope, A. W. Corals
699   concentrate dissolved inorganic carbon to facilitate calcification. *Nature*
700   *Communications* **5,** 5741 (2014).

701   60.   McCulloch, M. *et al.* Resilience of cold-water scleractinian corals to
702   ocean acidification: Boron isotopic systematics of pH and saturation
703   state up-regulation. *Geochimica et Cosmochimica Acta* **87,** 21–34
704   (2012).

705   61.   Gagnon, A. C., Adkins, J. F., Erez, J. & Eiler, J. M. Sr/Ca sensitivity to
706   aragonite saturation state in cultured subsamples from a single colony
707   of coral: Mechanism of biomineralization during ocean acidification.
708   *Geochemica et Cosmochimica Acta* **105,** 240–254 (2013).

709   62.   Rae, J. W. B. in *Boron Isotopes* 107–144 (2017).

710   63.   Wang, X. T. *et al.* Deep-sea coral evidence for lower Southern Ocean
711   surface nitrate concentrations during the last ice age. *PNAS* **114,** 3352–
712   3357 (2017).

713